MATERIALS PHYSICS AND MECHANICS RESEARCH ARTICLE

Submitted: September 23, 2025 **Revised: January 13, 2026** **Accepted: February 2, 2026**

Influence of rotational speed on performance metrics in friction stir lap welding of aluminium 6061 and stainless steel 304-CFD approach

A. Yadav ✉, **A. Jain, R. Verma**

NIT Kurukshetra, Kurukshetra, India

✉ amit.insan77@gmail.com

ABSTRACT

The joining of dissimilar materials such as aluminium and steel is of growing importance in modern manufacturing, owing to the demand for lightweight structures with superior mechanical performance. This study investigates the influence of rotational speed on key thermo-mechanical performance measures during dissimilar friction stir lap welding of aluminium alloy-6061 and stainless steel-304. Using finite volume method, numerical simulations were performed to quantify maximum weld interface temperature, maximum weld interface velocity, minimum weld interface viscosity, and tool-workpiece interface torque over a rotational speed range of 200–2200 rpm. Results reveal that maximum weld interface temperature rise steeply up to about 1000 rpm and then plateau due to thermal equilibrium. maximum weld interface velocity increases almost linearly with rotational speed, indicating improved interfacial shear and material mixing. In contrast, minimum weld interface viscosity and tool-workpiece interface torque decrease markedly as rotational speed increases, reflecting enhanced thermal softening and reduced resistance to tool motion. Intermediate rotational speed values (≈ 600–1200 rpm) provide an optimal balance of heat generation, material plasticization and torque, minimising the risk of excessive intermetallic compound growth or welding defects. The findings establish a physics-based framework for selecting process parameters that enhance joint integrity and efficiency in dissimilar friction stir lap welding of AA6061-SS304.

KEYWORDS

friction stir weld • computational fluid-dynamics • finite-volume approach • ANSYS • fluent

Citation: Yadav A, Jain A, Verma R. Influence of rotational speed on performance metrics in friction stir lap welding of aluminium 6061 and stainless steel 304-CFD approach. *Materials Physics and Mechanics*. 2026;54(1): 85–100. http://dx.doi.org/10.18149/MPM.5412026_9

Introduction

The automotive, aerospace, and marine industries necessitate lightweight structures with superior wear resistance to ensure optimal performance and durability [1]. These specific applications underscore hybrid structures combining lightweight materials such as aluminium (Al) with stainless steel (SS) [2]. Strategically utilising joints made from SS and Al alloys in critical areas provides a practical solution [3]. Various new joining techniques were employed by researchers for joining difficult-to-join and dissimilar materials [4–7]. Friction stir welding (FSW) pioneered and patented by "The Welding Institute UK" in 1991 stands as a promising solution, surpassing traditional fusion welding methods due to its advantages, including reduced heat input, thinner intermetallic compounds (IMCs), and enhanced surface properties [8–10]. FSW has advantages over fusion techniques for welding many metals, such as welding alloys of aluminium, titanium, copper, etc. [11].

Publisher: Peter the Great St. Petersburg Polytechnic University

In FSW, the spinning tool is gradually plunged into the workpiece until the shoulder comes into full contact. This position is maintained until the required temperature is reached, generated by frictional heating and plastic deformation. In order to accomplish the necessary weld, the tool is traversed along the weld line. The side of the rotating tool where the tangential velocity coincides with the traverse speed (TRS) is referred to as the advancing side (AS) [12]. The retreating side (RS) refers to the side of a rotating tool that has a vectorial sense opposite to the tangential velocity and TRS [12]. The workpiece section located ahead of tool is known as leading side, and the section located behind tool is known as trailing side [12]. FSW generates welds without the melting of the base material, hence eliminating the risks of solidification cracking, deformation, porosity, and other related issues. It necessitates no edge preparation and generates transition junctions between dissimilar metals [12].

The primary restriction of FSW is its necessity for distinct tools corresponding to varying workpiece thicknesses, and the resultant exit hole that remains upon the withdrawal of the tool from the workpiece. Large forces on clamp, necessitate robust gripping. It is primarily restricted to linear welding. Furthermore, filler joints are unattainable using FSW [12].

Recent research has largely focused on utilising FSW to repair defects in structural components, whereby friction stir techniques can effectively repair defects such as pores, cracks, grooves, through holes, and the like [13]. Since its inception, extensive research has focused on the influence of various process parameters in FSW [14,15]. These parameters govern heat transfer and material flow, thereby affecting the resulting microstructure and weld quality [16,17]. Achieving optimal welding performance requires careful evaluation of these parameters with respect to key thermo-mechanical measures, namely maximum weld interface temperature (MWIT), maximum weld interface velocity (MWIV), minimum weld interface viscosity (MWIVis), and tool-workpiece interface torque (TWIT) [18]. The present study investigates the effect of tool rotational speed (ROS) on MWIT, MWIV, MWIVis, and TWIT during dissimilar friction stir lap welding (DFSLW) of aluminium alloy 6061 (AA6061) and stainless steel 304 (SS304).

Literature review

In recent years, extensive research has examined the influence of process parameters on the performance of dissimilar friction stir welding (DFSW) of SS304 with various aluminium alloys. Nishida et al. [19] examined development of interfacial microstructures in dissimilar friction stir lap welding (DFSLW) between AA3003-H112 and SS304. Analysis of the bottom surface of the exit-hole showed that there were several mixed layers with ultrafine IMCs. The continuous thin reaction coating that was produced at the interface was also reported to be stronger than the base aluminium alloy. Habibnia et al. [20] researched the concept of microstructural and mechanical properties of dissimilar friction stir butt welds (DFSBW) in AA5050-SS304. Their findings indicated that joint quality increased with a lower tool rotational speed (ROS) and higher TRS.

Ghosh et al. [21] investigated the thermal impact on the microstructure of weld nugget of DFSBW of AA6061 and SS304. Higher heat contribution favored increasing the

iron content at the interface, changing IMC composition Fe_2Al_5 to more iron-rich grains in the Fe -Al phase diagram. At intermediate ROS, which was coincident with the formation of Fe_3Al and $FeAl_2$ phases, maximum microhardness and tensile strength were obtained. Balamagendiravarman et al. [22] compared the microstructure and mechanical behaviour of DFSBW of SS304 and commercial pure aluminium. There were minimal changes in microstructure on the steel surface in comparison to aluminium as a result of thermal and mechanical variation. In the interface and stir zone (SZ), Al_3Fe IMCs were observed, and the hardest point was at the SZ. The highest tensile was 78 percent of the aluminium base metal. The same authors in a follow-up study [23] demonstrated that addition of more ROS enhanced IMC layer thickness and facilitated the growth of $FeAl_2$, Fe_4Al_{13}, Fe_2Al_5 and $FeAl_3$. At 400 rpm, it reached the maximum joint efficiency of 90 % and elongation of 4.5 % and the maximum hardness was obtained in the SZ at the high ROS.

In the study by Mahto et al. [24], the practicality of underwater friction stir welding (UFSW) of AA6061 and SS304 was evaluated at different levels of ROS and plunge depth (PD). Less heat input and faster cooling in UFSW inhibited the excessive IMC, fine-tuned the weld microstructure and minimized defects including porosity, voids and kissing bonds leading to greater strength in the joints. They studied interfacial microstructure and corrosion behaviour of the DFSLW in a related study [25]. Reducing grain size was improved by the increasing ROS and the PD because of the rapid cooling and heating speeds. IMCs like Fe_2Al_5 and $AlCrFe_2$ were discovered and the corrosion resistance declined with reducing grain size mainly due to pitting and intergranular corrosion. The researchers of Chitturi et al. [26] investigated how tool tilt angle (TA) and pin depth influence DFSLW of AA5052 and SS304. Low TAs (0° and 1.5°) were found to have tunnel defects and micro-voids whereas defect-free joints were obtained at 2.5° owing to enhanced mixing of the material and formation of IMC. Both sides of the weld have hooks that improved mechanical interlocking and the SZ hardness was almost three times greater than SS304.

Uematsu et al. [27] carried out crack propagation tests on DFSBW joint of AA6061 and SS304. The rates of fatigue crack propagation of the welds were also lower than that of the aluminium base metal and when compared by the effective stress intensity factor range of the fatigue crack propagation, the behavior of the fatigue crack propagation was similar in all the samples. Chitturi et al. [28] also tested the fracture behavior of DFSLW of AA5052 and SS304 at different TAs, ROS, TRS, and PDs. Fractures that were mainly initiated on the aluminium side had mixed brittle-ductile failure modes. X-ray diffraction was used to confirm the formation of AlFe based IMCs, and hardness was found to be between 300–630 HV with different process conditions. Jabraeili et al. [29] examined the effect of the welding parameters on DFSBW of AA2024 and SS304. Tool offset was found to be a vital parameter whereby with positive offsets one will end up with tunnel defects because the heat input was not enough and in the case of negative offsets thick IMC layers were produced. The finest conditions gave a serrated interface of thin IMCs and increased strength and ductility of the joints.

Wang et al. [30] have compared the microstructure and mechanical behavior of AA3003 and SS304 DFSBW joints. Tool offset was more significant compared to ROS on the microstructure of the joints. Reduced ROS enhanced tensile strength and hardness

with a constant offset, and the start of a failure was at the weld root and spread through the SZ. The authors of Joshani et al. [31] were researching the DFSBW of AA7075, and SS304 at various ROSs. The increment of ROS enhanced the IMC thickness to 6 μm and diminished joint strength. Optimal tensile strength (about 72 % AA7075) was realized at the lower ROS, whereas fracture moved to the SZ at the higher ROS. Datta et al. [32] made comparisons between DFSBW of DAA1100, and DAA7075 and that of SS304. Joint AA1100 -SS304 was more efficient and ductile. The reduced traverse velocity improved strength and elongation because of the controlled amount of heat.

Kumar et al. [33] examined DFSBW of AA7075 and SS304 and stated that the higher the ROS, the greater was the heat generation leading to thicker IMC layers and less tensile strength. The refinement of the grains was also great, which resulted in equiaxed recrystallized grains and IMCs like $Al_{13}Fe_4$, Al_3Fe_2, and Al_3Mg_2 at the interface. Ou et al. [34] have constructed the model of heat transfer in DFSBW of AA6061 and SS304, to include the welding tool. The model determined peak temperatures with a margin of error of 2.3 % and showed low temperature gradients and IMC thickness at increasing TRSs. DFSBW of SS304 and AA2024-T3 was well investigated by Mir et al. [2,10,35]. Their results pointed to better wear and corrosion resistance, refinement of grains, and hardness in the stir zone with the best heat input and material flow. Zhang et al. [36] were able to obtain defect free DFSBW of SS304 and AA2219 with low ROS at 200 rpm. Substantiation of thin amorphous Al Fe O layer inhibited the Cu rich IMCs yielding high metallurgical bonding and tensile strength of 210 MPa. Nakrani et al. [37] examined fatigue cracking characteristics in DFSBW of SS304 and AA5083, which showed an increased rate of crack propagation at the Al-steel interface, and brittle fractures behavior at the interface. Caetano et al. [38] investigated DFSBW of SS304 and SS410, demonstrating that placing ferritic SS410 on the AS reduced flash formation and voids. Increased axial force eliminated root defects, although it promoted higher flash formation on the AS.

Overall, prior research on DFSW between aluminium alloys and stainless steel has primarily concentrated on interfacial microstructural evolution, IMC formation, and mechanical performance. While studies have highlighted the role of parameters such as ROS, TRS, PD, TA, and welding environment, significant research gaps remain. In particular:

1. The effect of ROS on critical thermo-mechanical performance measures (MWIT, MWIV, MWIVis, and TWIT) has not been systematically quantified.
2. Weld interface viscosity, a key factor governing material flow, mixing, and defect formation, remains underexplored in dissimilar lap welds of AA6061-SS304.
3. Torque variation with ROS and its correlation with weld quality in AA6061-SS304 lap welds have not been addressed.

Most existing studies emphasise butt joints or other aluminium alloys (AA2024, AA5052, AA7075), leaving the practically relevant AA6061-SS304 lap configuration insufficiently studied. To address these gaps, the present work employs a physics-based finite volume method (FVM) simulation using ANSYS® Fluent® to analyse the effect of ROS on MWIT, MWIV, MWIVis, and TWIT in DFSLW of AA6061-SS304. This systematic investigation provides deeper insights into heat generation, material flow, and tool-workpiece interaction, offering a framework to minimise defects and improve joint efficiency.

Simulation design

The simulation model utilises an AA6061 sheet and an SS304 sheet with dimensions of 200 × 75 × 3 mm^3 (each sheet). They are joined in a lap arrangement with an overlap width of 30 mm (Fig. 1). Solidworks® 2017 is used for geometric modelling, while CFD software ANSYS® 19.3 R3 (FLUENT®) is employed for FVM numerical simulation [39]. A flat shoulder tool with a frustum conical pin is employed (Table 1).

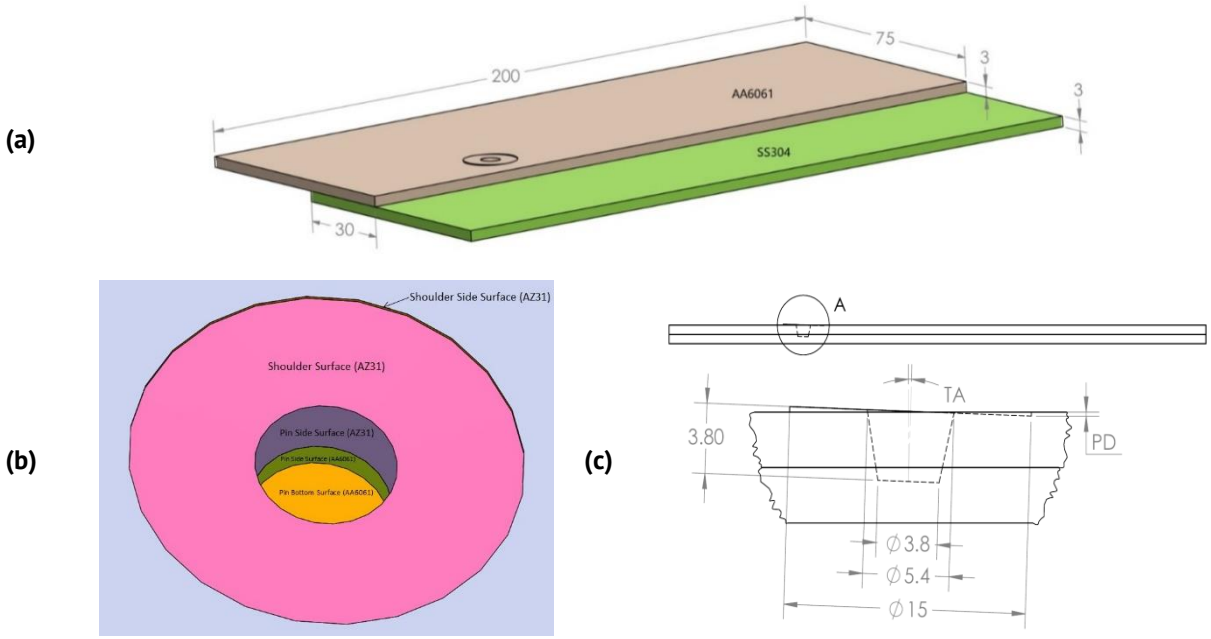

Fig. 1. (a) Arrangement of dissimilar friction stir lap weld of AA6061 with SS304; (b) tool-workpiece interface surfaces; (c) dimensions of tool employed

Table 1. Fixed process parameters

Process parameter	Value
Diameter of flat shoulder, mm	15
Pin length, mm	3.8
Pin base diameter, mm	5.4
Pin tip diameter, mm	3.8
PD, mm	0.225
TA	1.5°
Overlap width, mm	30

The Realisable k-epsilon viscous model is employed to simulate the flow of material in a transient state [40]. Mesh with tetrahedral elements (899766 in numbers) and 187342 nodes are utilised, with fine mesh at the interface between the tool and the workpiece, as depicted in Fig. 2 [41]. The present work adheres to the following assumptions:

1. The process is a quasi-steady process, i.e., the rate of heat generation remains constant.
2. Material that has undergone plasticization is classified as non-Newtonian, incompressible, and visco-plastic.
3. The material is presumed to exhibit characteristics of a non-Newtonian fluid, where its viscosity is influenced by both temperature and strain rate.

4. Partial slip condition exists between the tool and the workpiece.
5. Free slip condition exists on the upper, bottom, and side surfaces of the workpiece.
6. The outlet boundary assumes the value of zero pressure.

To make precise predictions about welding, it is crucial to employ realistic boundary conditions [42,43]. Figure 3 displays the parts and boundaries imposed on the model. The inlet boundary condition of flow is defined as follows:

$$u = u_{weld}, v = 0, w = 0, \quad (1)$$

where the TRS is represented by u_weld, whereas the velocity intensities in the X, Y, and Z directions are represented by u, v, and w, respectively.

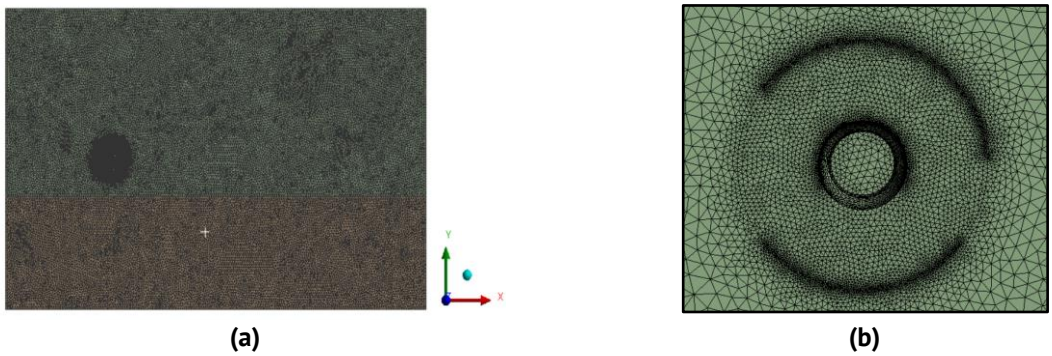

Fig. 2. (a) Tetrahedron cells' mesh used in the model; (b) close up view (top) of tool-workpiece interface

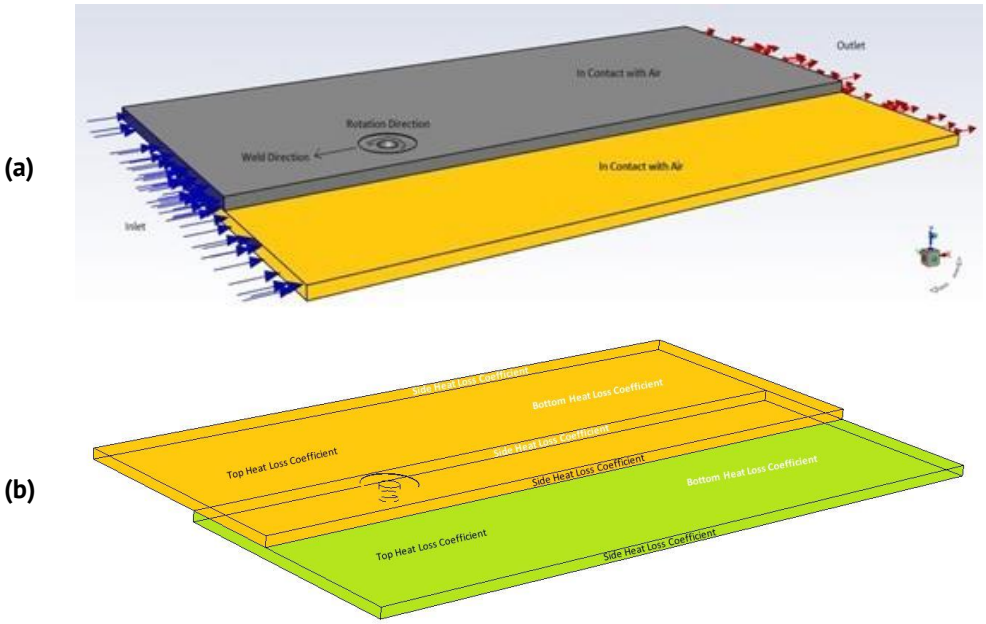

Fig. 3. (a) Flow directions of materials in the model; (b) different heat loss surfaces of the model

The tool periphery velocity, which is the combined effect of tool's ROS and TRS, is provided below:

$$u_i = \omega r sin\theta - u_{weld},$$
$$v_i = \omega r cos\theta, \quad (2)$$
$$w_i = 0.$$

The value of r is such that $r_1 < r < r_3$. The variables u_i, v_i and w_i denote vectors of velocity in the X, Y, and Z directions. The index notation "i" means a specific location on tool's surface where the tool's combined ROS and the TRS are determined. r_1 represents the radius of tool shoulder; r_3 represents the radius of pin bottom; θ is the angle between the horizontal direction vector from the tool axis to any point on the cylindrical surface. In the weld direction, θ is equal to zero.

Tool periphery velocity when tool TA (ξ) and contact state variable (δ) are considered, are represented by equations below [44]. Equations (3)–(5) are used to define the momentum boundary conditions at the tool-workpiece interface, specifically at the shoulder surface (SS), pin side surface (PSS), and pin bottom surface (PBS).

$$u_i = (1-\delta)(\omega r sin\theta)\cos\xi - u_{weld}, \quad (3)$$

$$v_i = (1-\delta)\omega r cos\theta, \quad (4)$$

$$\mathrm{w_i} = (1-\delta)(\omega \mathrm{r sin\theta})\sin\xi, \quad (5)$$

$$\delta_{AA6061} = \left(0.31e^{\omega r/1.87} - 0.026\right) \text{ (from [45])}, \ \delta_{SS304} = 0.7 \text{ (from [46])}. \quad (6)$$

The viscosity (η), flow stress (σ), Zener Hollomon parameter (Z) and strain rate ($\bar{\varepsilon}$) are determined using the equations below [47–49]:

$$\eta = \frac{\sigma}{3\bar{\varepsilon}}, \quad (7)$$

$$\sigma = \frac{1}{\beta}\ln\left\{\left(\frac{Z}{A}\right)^{\frac{1}{n}} + \left(1+\left(\frac{Z}{A}\right)^{\frac{2}{n}}\right)^{\frac{1}{2}}\right\}, \quad (8)$$

$$Z = \bar{\varepsilon}\mathrm{e}^{\left(\frac{Q}{RT}\right)}, \quad (9)$$

$$\bar{\varepsilon} = \left(\frac{2}{3}\varepsilon_{ij}\varepsilon_{ij}\right)^{\frac{1}{2}}, \quad (10)$$

where T represents temperature, measured in Kelvin (K), A, β, and n are constants that describe the material properties, Q is an activation energy that does not depend on temperature, R is the gas constant (8.314 J·K^{-1}·mol^{-1}).

Table 2. Material-constants and properties for AA6061 and SS304 [44,46,51–53]

Parameters		**AA6061**	**SS304**
Material constants	A, s^{-1}	2.41 × 10^8	1.62 x 10^{16}
	n	3.55	6.1
	Q, J·mol^{-1}	1.45 × 10^5	4.46 x 10^5
	β, MPa^{-1}	0.0367	0.008
Material density ρ, kg·m^{-3}		2700	7400
Top (h_t) & side (h_s) heat transfer coefficient, W/m^{2}K		80	0.0668T
Bottom (h_b) heat transfer coefficient, W/m^{2}K		150	10*0.0668T
External emissivity of workpiece top surface		0.09	0.17

Table 2 provides the material constants and properties of AA6061 [50]. Equation (7) is used to define the viscosity as a function of temperature and strain rate for the given materials, namely AA6061 and SS304. These equations are implemented through the use of user defined functions.

The heat created during the FSW process is distributed over many regions. The tool's contacting surface with the workpiece is partitioned into three sections: bottom SS, P_{SS}, and P_{BS}. The SS is subdivided into two sections: shoulder with conical surface

(S_{CS}) and shoulder with flat surface (S_{FS}). All these sections exhibit partial sticking-sliding contact. Heat produced by different sources is provided underneath:

$$Q_{total} = \delta Q_{sticking} - (1-\delta) Q_{sliding}. \quad (11)$$

When the slip coefficient (δ) is equal to zero, heat is only generated through friction. When the value of δ is equal to 1 (indicating a stick), all heat is produced only through the deformation of the plastic material [54].

The assumed maximum yielding shear stress is [55]:

$$\tau_b = \frac{\sigma_s}{\sqrt{3}}, \quad (12)$$

$$(\sigma_s)_{AA6061} = 1160 - 8.88T + 2.97 \times 10^{-2} T^2 - 3.32 \times 10^{-5} T^3 \text{ (from [52])}, \quad (12a)$$

$$(\sigma_s)_{SS304} = 796 - 1.6T + 2.25 \times 10^{-3} T^2 - 1.3 \times 10^{-6} T^3 \text{ (from [46])}, \quad (12b)$$

where σ_s represents the material's yield stress.

The heat-flux (W/m^2) in S_{CS} section is [44,46,51,52]:

$$q_{S_{CS}} = \eta \left(\frac{[(1-\delta_{CSS})\tau_b + (\delta_{CSS})\mu P] 2\omega [(r_1^3 - r_2^3)(1+\tan\propto')]}{3(r_1^2 - r_2^2)} \right). \quad (13)$$

The heat-flux (W/m^2) in P_{SS} section is:

$$q_{P_{SS}} = \eta((\omega r - v sin\theta)((1-\delta_{PSS})\tau_b + (\delta_{PSS})\mu P)). \quad (14)$$

The heat-flux (W/m^2) in P_{BS} section is:

$$q_{P_{BS}} = \eta \left(\frac{2\omega r_3 ((1-\delta_{PBS})\tau_b + (\delta_{PBS})\mu P)}{3} \right), \quad (15)$$

where μ (0.4 is same for both material) is the coefficient of friction [46,56], P is plunge pressure (Pa), ω is ROS (rad/s), η is fraction of heat transferred to the workpiece (i.e., 0.6 and 0.4 for AA6061 and SS304, respectively [34]), and $\propto'$ is cone angle of shoulder ($\propto'$ = 0 for S_{FS})). Plunging pressure of 12 and 109 MPa are taken for AA6061 and SS304, respectively [46,56]. Equations (13)–(15) are used to define the thermal boundary conditions for the SS, P_{SS}, and P_{BS}, respectively.

The specific heat (C_p) equation for AA6061 is shown below [45,46]:

$$(C_p)_{AA6061} = 929 - 0.627T + 1.481 \times 10^{-3} T^2 - 4.33 \times 10^{-8} T^3, \quad (16a)$$

$$(C_p)_{SS304} = 276 + 0.851T - 8.51 \times 10^{-4} T^2 + 3.0 \times 10^{-7} T^3. \quad (16b)$$

The thermal conductivity (k) equation for AA6061 is shown below [45,46]. Equations (16) and (17) are used to define C_p and k, respectively, as material properties for both AA6061 and SS304:

$$k_{AA6061} = 25.22 + 0.3978T + 7.358 \times 10^{-6} T^2 - 2.518 \times 10^{-7} T^3, \quad (17a)$$

$$k_{SS304} = 14.3 - 9.02 \times 10^{-3} T + 4.52 \times 10^{-5} T^2 - 2.49 \times 10^{-8} T^3. \quad (17b)$$

The boundary condition for heat exchange between the top surface of the workpiece and the environment is convective as well as radiative heat transfer [44]. The heat exchange between the bottom and side surfaces of the workpiece is conductive (due to contacts of jigs and fixtures) and convective heat transfer, respectively. All these heat exchanges are converted to convective form as shown below [44]:

$$k \frac{\partial T}{\partial z} = h_t (T - T_0), \quad (18)$$

$$k \frac{\partial T}{\partial z} = h_b (T - T_0), \quad (19)$$

$$k \frac{\partial T}{\partial z} = h_s (T - T_0), \quad (20)$$

where h_t, h_b and h_s are coefficients of heat dissipation at workpiece's top, bottom and side surface, respectively, T_0 is the environmental temperature (300 K) [45]. Equations (18)–(20)

are used to define the thermal boundary conditions for the workpiece's top surface, bottom surface, and side surface, respectively.

Validation of the current model is done with the work by Ou et al. [34]. A 3D CFD model was constructed to study the heat transfer in DFSBW of AA6061 with SS304 with a frustum conical pin tool. In the present study, the above work is replicated, and upon validation of the current methodology and procedure, additional fixed input parameters (TA and PD) are introduced. The temperature distribution data of the model closely corresponds to the experimental data of Ou et al. [34]. Table 3 compares the temperature of the experimental and model. Thus, the numerical modelling method is satisfactory.

Table 3. Comparison results between experimental and modelled temperature

Points (approx.)	Experimental temperature [34], K	Simulation model temperature, K	Error, %
p1 (8.99,0.5,3)	492.3	469.6	4.61
p2 (8.94,1,3)	475.1	455.3	4.16
p3 (-8.06,4,3)	439.4	429.4	2.27

Results and Discussion

This section examines the influence of ROS on the performance measures MWIT, MWIV, MWIVis, and TWIT. The ROS range is selected between 200 and 2200 rpm, based on findings from the literature. To evaluate the effect of ROS on the above performance indicators, all other process parameters: TRS, TA and PD, are maintained constant at 100 mm/min, 1.5°, and 0.225 mm, respectively. Table 4 presents the corresponding performance measures for the investigated ROS range of 200 to 2200 rpm. Simulation experiments were conducted for various values of ROS as process parameters to compute MWIT, MWIV, MWIVis, and TWIT performance measures for each. Columns 4–7 of Table 4 indicate the MWIT, MWIV, MWIVis, and TWIT obtained in each experiment, respectively. The analysis of results is discussed below.

Table 4. Experimental design and its results

S.No.	ROS, rpm	Max. workpiece temperature, K	MWIT, K	MWIV, m/s	MWIVis, kg/(ms)	TWIT, Nm
1	200	533	469	0.0133	3.16E+07	16.14
2	400	691	558	0.0266	1.21E+07	16.06
3	600	809	626	0.0399	4.01E+06	15.99
4	800	890	675	0.0532	2.57E+06	15.82
5	1000	942	722	0.0666	1.45E+06	15.12
6	1200	977	756	0.0799	1.08E+06	14.74
7	1400	1000	785	0.0932	9.83E+05	14.34
8	1600	1017	808	0.1065	9.56E+05	14.04
9	1800	1014	826	0.1199	8.82E+05	13.76
10	2000	1016	829	0.1332	7.50E+05	13.49
11	2200	1018	833	0.1465	6.90E+05	13.26

Effect of ROS on MWIT

From Fig. 4, it is observed that both MWIT and maximum workpiece temperature increase with increasing ROS up to a certain point, after which they tend to stabilise. At lower ROSs (200–600 rpm), a steep rise in both temperatures is noted, indicating that heat generation is highly sensitive to ROS in this range. For instance, MWIT increases from 469 K at 200 rpm to 626 K at 600 rpm, while the maximum workpiece temperature rises from 533 to 809 K over the same range. This behaviour can be attributed to enhanced frictional heat and plastic deformation as the tool speed increases [57].

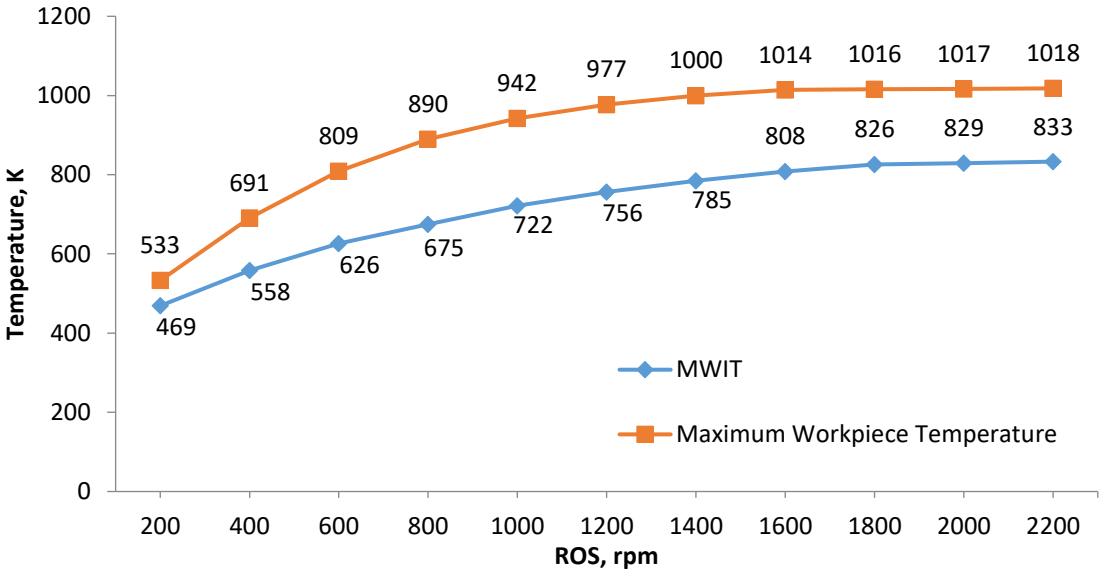

Fig. 4. Effect of ROS process parameter on MWIT performance measure

Beyond ~ 1000 rpm, the temperature curves show a tendency to plateau. The maximum workpiece temperature reaches about 1018 K at 2200 rpm, while MWIT stabilises around 833 K. This saturation effect occurs because, at higher ROSs, the heat dissipation rate through conduction and convection counterbalances the additional heat input, preventing further significant temperature rise [58].

A consistent observation is that the maximum workpiece temperature remains higher than the MWIT across all ROSs. This is expected since the bulk workpiece accumulates heat from both frictional sliding and plastic deformation, whereas the weld interface experiences localised heat generation that is partly dissipated into the adjoining materials [59].

Implications for weld quality: the progressive rise in temperature with increasing ROS enhances diffusion and reaction kinetics at the AA6061-SS304 interface, promoting IMC layer formation. However, excessive IMC growth at higher temperatures may lead to brittle phases, reducing joint toughness [60,61].

Moderate ROS values (600–1200 rpm) provide sufficient thermal softening and material flow without excessive IMC growth, which is favourable for achieving high-strength welds [60,61]. At very low ROS, inadequate heat input results in poor plasticization and insufficient bonding, while excessively high ROS (beyond ~ 1600 rpm) risks overheating,

excessive flash formation, or void generation [60,61]. Thus, selecting an optimal ROS range is critical for balancing heat input, material flow, and metallurgical reactions.

Effect of ROS on MWIV

Figure 5 graph presents the variation of MWIV with ROS. It is evident that MWIV increases almost linearly with increasing ROS. At the lowest speed of 200 rpm, MWIV is only 0.0133 m/s, while at the highest speed of 2200 rpm, it reaches 0.1465 m/s, representing more than a tenfold increase. This strong positive correlation reflects the direct dependence of interface velocity on tool rotation, since higher ROS enhances the relative tangential velocity between the tool and the workpiece (from Eqs. (3)–(5)).

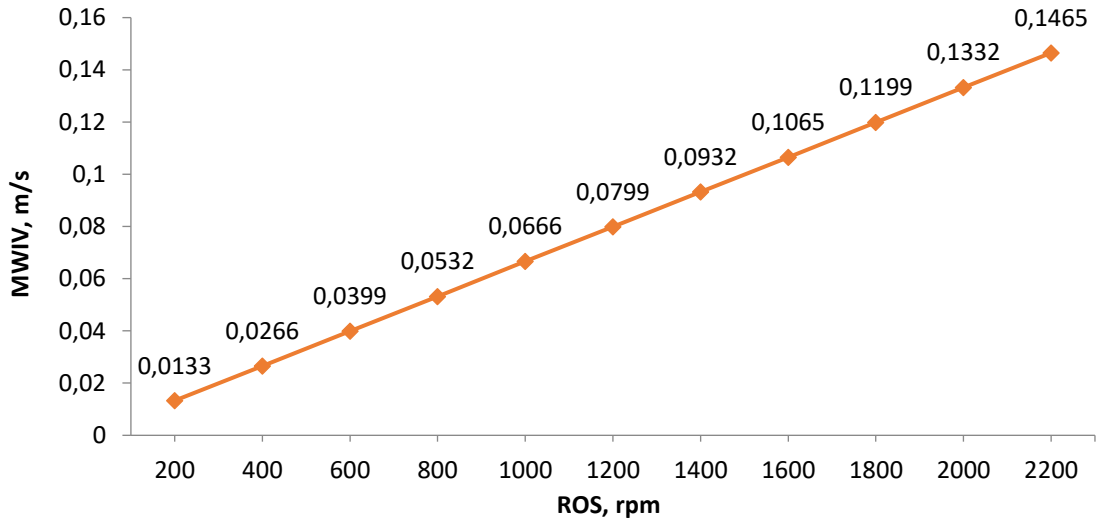

Fig. 5. Effect of ROS process parameter on MWIV performance measure

The nearly linear trend also indicates that material flow at the weld interface scales proportionally with tool speed, without showing saturation or instability within the investigated range. This suggests that ROS is the dominant driver of weld interface shear velocity, which in turn influences plastic deformation, material mixing, and bonding efficiency [62–64]. Therefore, tool speed is sometimes referred to as ROS.

Implications for weld quality: higher MWIV at increased ROS promotes improved plasticization and mixing of AA6061 and SS304 at the interface, which is essential for sound metallurgical bonding [57,63]. Since frictional heating is directly linked to interface velocity, the rising MWIV also complements the increase in weld interface and workpiece temperatures, ensuring sufficient softening for weld formation [62,65]. While low MWIV (at lower ROS) can result in insufficient stirring and weak bonding, excessively high MWIV (at very high ROS) may lead to turbulent flow, uneven mixing, or excessive flash, thereby compromising weld integrity [57,63].

Effect of ROS on MWIVis

A distinct decreasing trend is observed from Fig. 6, where MWIVis reduces rapidly with an increase in ROS up to approximately 1200 rpm, after which the values stabilise with

minimal further reduction. At lower rotational speeds (200–600 rpm), extremely high viscosity values are recorded, such as 3.16E+07 kg/ms at 200 rpm and 1.21E+07 kg/ms at 400 rpm. These high viscosities indicate inadequate heat generation, resulting in poor material plasticization and insufficient mixing at the weld interface [63].

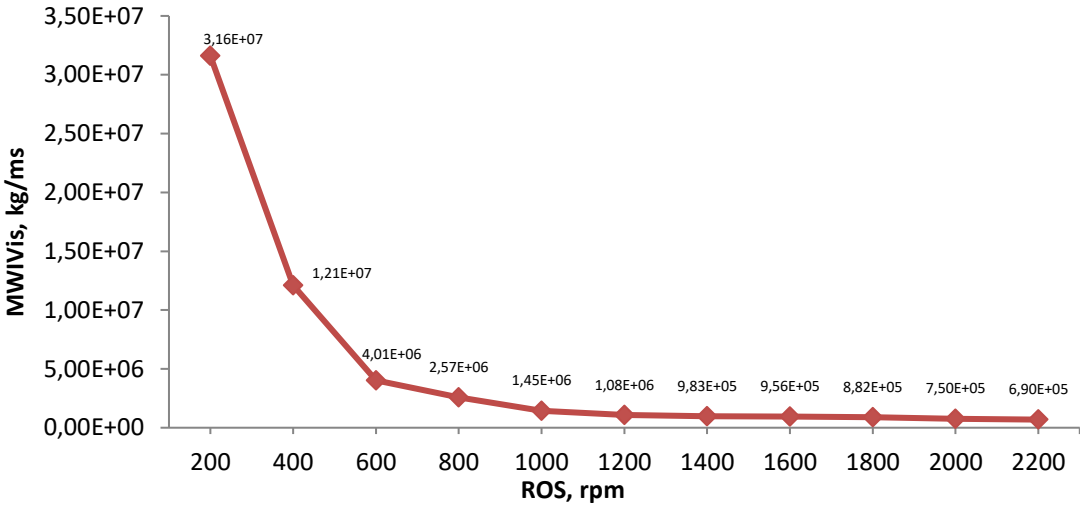

Fig. 6. Effect of ROS process parameter on MWIVis performance measure

As the ROS increases into the intermediate range (600–1200 rpm), MWIVis decreases sharply, reaching values around the order of 106 kg/ms. This reduction highlights the improved thermal softening of the workpiece materials, which enhances plastic flow and promotes effective interfacial bonding [57].

At higher ROSs (1400–2200 rpm), MWIVis values stabilise in the range of 9.83E+05 to 6.90E+05 kg/ms. This plateau suggests that beyond a certain threshold, additional increases in ROS do not significantly improve material plasticization, as the system achieves a thermal equilibrium. Excessively high speeds may therefore lead to diminishing improvements in weld quality while potentially accelerating tool wear and energy consumption [57].

Implications for weld quality: optimal joint formation is likely achieved in the intermediate to moderately high ROS range (1200–1600 rpm), where sufficient heat is generated to ensure effective mixing without excessive thermal input that could cause grain coarsening, intermetallic growth, or tool wear [57,63]. ROS directly governs interface viscosity, which in turn dictates weld strength, microstructural refinement, and overall joint performance [57,63].

Effect of ROS on TWIT

A clear decreasing trend is observed from Fig. 7, where TWIT gradually declines from 16.14 Nm at 200 rpm to 13.26 Nm at 2200 rpm. At lower ROSs (200–800 rpm), TWIT remains relatively high (≈16 Nm), indicating that greater torque is required to overcome the resistance to tool penetration and material flow due to limited heat generation and higher viscosity of the workpiece [57,58]. As the ROS increases, TWIT steadily decreases, dropping to 15.12 Nm at 1000 rpm and further to 14.04 Nm at 1600 rpm.

This reduction corresponds to enhanced softening of the material with increasing ROS, as higher frictional heating lowers viscosity and reduces the mechanical resistance encountered by the tool [57,58].

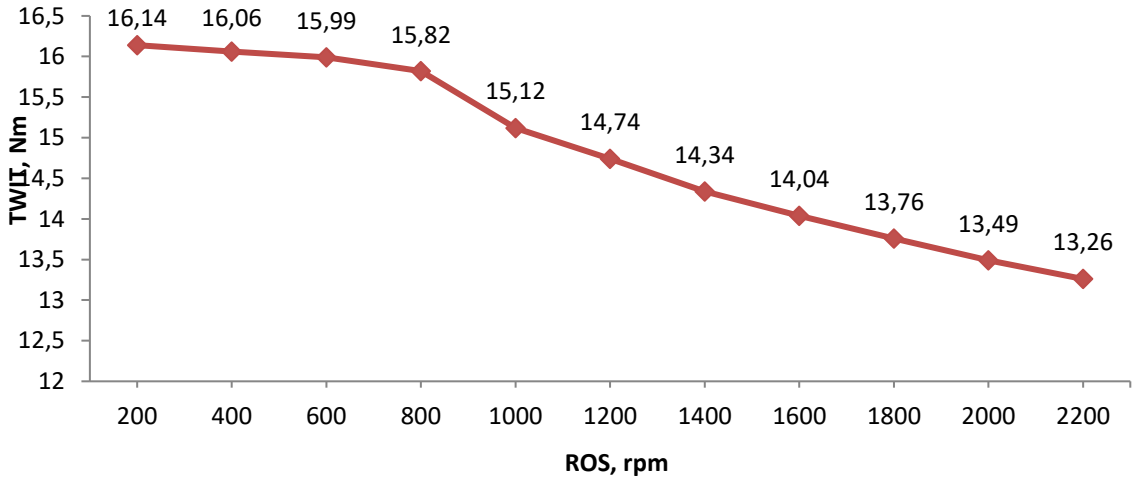

Fig. 7. Effect of ROS process parameter on TWIT performance measure

At higher ROSs (1800–2200 rpm), TWIT stabilises in the lower range of 13.76–13.26 Nm, suggesting that the system approaches thermal equilibrium where additional increases in ROS do not substantially reduce resistance to tool rotation (insufficient forging pressure at the weld interface, potentially leading to reduced consolidation, defect formation, or weaker interfacial bonding may occur) [57,58].

Implications for weld quality: at lower speeds, higher torque values indicate that the tool faces greater resistance due to insufficient heat generation and higher material viscosity. This condition often leads to poor material flow, incomplete mixing, and defect formation at the weld interface [57,58,63].

As the rotational speed increases, the decrease in torque reflects improved thermal softening and reduced flow resistance, which enhances material plasticization and promotes more uniform bonding [57,58,63]. However, excessively low torque values at very high speeds may result in inadequate forging pressure and insufficient compaction of plasticised material, which can compromise interfacial strength [57,58,63].

Conclusions

Numerical simulation of AA6061-SS304 DFSLW has demonstrated that tool ROS strongly governs the weld's thermo-mechanical behaviour:

1. MWIT and overall workpiece temperature initially rise sharply with increasing ROS before stabilising, while MWIV shows a nearly linear increase across the studied range.
2. Conversely, MWIVis and TWIT decrease significantly as ROS increases, highlighting the combined effects of frictional heating and improved material flow.
3. An intermediate ROS window of roughly 600–1200 rpm yields sufficient thermal softening and interfacial mixing without excessive intermetallic compound formation or loss of forging pressure.

These insights provide a quantitative basis for optimising DFSLW process parameters to produce defect-free, high-strength joints and to improve energy efficiency in industrial applications involving aluminium-steel hybrid structures.

CRediT authorship contribution statement

Amit Yadav: writing – original draft, conceptualization, investigation, data curation; **Ajai Jain**: writing – review & editing, supervision, data curation; **Rajiv Verma**: writing – review & editing, conceptualization, supervision, data curation.

Conflict of interest

The authors declare that they have no conflict of interest.

References

1. Tisza M, Czinege I. Comparative study of the application of steels and aluminium in lightweight production of automotive parts. *International Journal of Lightweight Materials and Manufacture*. 2018;1(4): 229–238.
2. Mir FA, Khan NZ, Nisar L, Khan HA, Alrokayan SH. Analyzing microstructural evolution and wear behavior of friction stir welded dissimilar joints of SS304 and 2024-T3 Al alloy. *Materials Letters*. 2024;366: 136493.
3. Kusuda Y. Honda develops robotized FSW technology to weld steel and aluminum and applied it to a mass-production vehicle. *Industrial Robot: An International Journal*. 2013;40(3): 208–212.
4. Lazarević M, Bajić DM, Marinković J, Alil A. Cavitation resistance of explosively welded aluminium/steel joint. *Tribology and Materials*. 2024;3(2): 67–72.
5. Damlacik S, Baydi Z, Küpeli S, Kaplan D, Akan RŞ, Uludağ M. Study on mechanical and microstructural properties of advanced high-strength welded sheet metal. *Tribology and Materials*. 2023;2(2): 68–77.
6. Klobčar D, Pušavec F, Bračun D, Garašić I, Kožuh Z, Vencl A, Trdan U. Influence of Friction Riveting Parameters on the Dissimilar Joint Formation and Strength. *Materials*. 2022;15(19): 6812.
7. Milašinović V, Alil A, Milašinović M, Vencl A, Hatala M, Dikić S, Gligorijević B. Continuous Drive Friction Welded Al/Cu Joints Produced Using Short Welding Time, Elevated Rotational Speed, and High Welding Pressures. *Materials*. 2024;17(13): 3284.
8. Tsang S. Friction welding. In: Olson DL, Siewert TA, Liu S, Edwards GR. (eds.) *ASM Handbook. Volume 6: Welding, Brazing and Soldering*. Materials Park (OH): ASM International; 1993. p.315–317.
9. Heidarzadeh A, Mironov S, Kaibyshev R, Çam G, Simar A, Gerlich A, Khodabakhshi F, Mostafaei A, Field DP, Robson JD, Deschamps A, Withers PJ. Friction stir welding/processing of metals and alloys: A comprehensive review on microstructural evolution. *Progress in Materials Science*. 2021;117: 100752.
10. Mir FA, Khan NZ, Parvez S, Siddiquee AN. Investigations on surface properties of friction stir welded dissimilar AA2024-T3 and 304 stainless steel joints. *Tribology International*. 2024;193: 109312.
11. Elmetwally HT, Abdelhafiz MA, Mahmoud E, El-Sheikh SA, Abdullah AA. Effect of Friction Stir-Welding Tool Pin Geometry on the Characteristics of Al-Cu Joints. *Applied Engineering Letters*. 2023;8(2): 60–69.
12. Nandan R, DebRoy T, Bhadeshia HKDH. Recent advances in friction-stir welding: Process, weldment structure and properties. *Progress in Materials Science*. 2008;53(6): 980–1023.
13. Lakli B, Berrahou M, Serier M. Temperature and Plastic Strain Evaluation during Friction Stir Repair of Corrosion Defects in Al2024. *Applied Engineering Letters*. 2025;10(1): 25–34.
14. Sun Z, Wu CS, Kumar S. Determination of heat generation by correlating the interfacial friction stress with temperature in friction stir welding. *Journal of Manufacturing Processes*. 2018;31: 801–811.
15. Zhai M, Wu CS, Su H. Influence of tool tilt angle on heat transfer and material flow in friction stir welding. *Journal of Manufacturing Processes*. 2020;59: 98–112.
16. Jain R, Pal SK, Singh SB. A study on the variation of forces and temperature in a friction stir welding process: A finite element approach. *Journal of Manufacturing Processes*. 2016;23: 278–286.
17. Shi L, Wu CS. Transient model of heat transfer and material flow at different stages of friction stir welding process. *Journal of Manufacturing Processes*. 2017;25: 323–339.

18. Kamalvand E, Jabbari A, Reza SM, Mazdak S, Beygi R, Mohammadi S. Effect of friction stir welding parameters on the deep drawing of tailor-welded blanks (TWBs). *CIRP Journal of Manufacturing Science and Technology*. 2021;33: 91–99.
19. Nishida T, Ogura T, Nishida H, Fujimoto M, Takahashi M, Hirose A. Formation of interfacial microstructure in a friction stir welded lap joint between aluminium alloy and stainless steel. *Science and Technology of Welding and Joining*. 2014;19(7): 609–616.
20. Habibnia M, Shakeri M, Nourouzi S, Givi MKB. Microstructural and mechanical properties of friction stir welded 5050 Al alloy and 304 stainless steel plates. *The International Journal of Advanced Manufacturing Technology*. 2015;76: 819–829.
21. Ghosh M, Gupta RK, Husain MM. Friction stir welding of stainless steel to Al alloy: Effect of thermal condition on weld nugget microstructure. *Metallurgical and Materials Transactions A*. 2014;45: 854–863.
22. Balamagendiravarman M, Kundu S, Chatterjee S. An analysis of microstructure and mechanical properties on friction stir welded joint of dissimilar 304 stainless steel and commercially pure aluminium. *Archives of Metallurgy and Materials*. 2017;62(3): 1813–1817.
23. Murugan B, Thirunavukarasu G, Kundu S, Kailas SV, Chatterjee S. Interfacial Microstructure and Mechanical Properties of Friction Stir Welded Joints of Commercially Pure Aluminum and 304 Stainless Steel. *Journal of Materials Engineering and Performance*. 2018;27: 2921–2931.
24. Mahto RP, Gupta C, Kinjawadekar M, Meena A, Pal SK. Weldability of AA6061-T6 and AISI 304 by underwater friction stir welding. *Journal of Manufacturing Processes*. 2019;38: 370–386.
25. Mahto RP, Anishetty S, Sarkar A, Mypati O, Pal SK, Majumdar JD. Interfacial Microstructural and Corrosion Characterizations of Friction Stir Welded AA6061-T6 and AISI304 Materials. *Metals and Materials International*. 2019;25: 752–767.
26. Chitturi V, Pedapati SR, Awang M. Effect of tilt angle and pin depth on dissimilar friction stir lap welded joints of aluminum and steel alloys. *Materials*. 2019;12(23): 3901.
27. Uematsu Y, Kakiuchi T, Ogawa D, Hashiba K. Fatigue crack propagation near the interface between Al and steel in dissimilar Al/steel friction stir welds. *International Journal of Fatigue*. 2020;138: 105706.
28. Chitturi V, Pedapati SR, Awang M. Investigation of weld zone and fracture surface of friction stir lap welded 5052 aluminum alloy and 304 stainless steel joints. *Coatings*. 2020;10(11): 1062.
29. Jabraeili R, Jafarian HR, Khajeh R, Park N, Kim Y, Heidarzadeh A, Eivani AR. Effect of FSW process parameters on microstructure and mechanical properties of the dissimilar AA2024 Al alloy and 304 stainless steel joints. *Materials Science and Engineering A*. 2021;814: 140981.
30. Wang J, Ling X, Zhang W, Lu X, Chen C. Microstructures and mechanical properties of friction stir welded butt joints of 3003-H112 aluminum alloy to 304 stainless steel used in plate-fin heat exchanger. *Journal of Materials Research and Technology*. 2022;21: 3086–3097.
31. Joshani E, Beidokhti B, Davodi A, Amelzadeh M. Evaluation of dissimilar 7075 aluminum/AISI 304 stainless steel joints using friction stir welding. *Journal of Alloys and Metallurgical Systems*. 2023;3: 100017.
32. Datta A, Shrivastava A, Mandal N, Roy H, Chakraborty SS. A comparative investigation of butt friction stir welding of aluminium alloys, AA 1100 and AA 7075, with AISI 304 stainless steel. *Welding in the World*. 2023;67: 1449–1465.
33. Kumar R, Manjaiah M, Davidson MJ. The effect of friction stir welding on the microstructure and mechanical properties of the dissimilar SS304 and Al7075-T6 alloy joints. *Welding International*. 2023;37(11): 643–654.
34. Ou W, Guo G, Cui C, Zhang Y, Qian L. Heat transfer in aluminum-steel joint and weld tool during the friction stir welding: Simulation and experimental validation. *The International Journal of Advanced Manufacturing Technology*. 2023;125: 2211–2224.
35. Mir FA, Khan NZ, Mukhtar Z, Badruddin IA, Kamangar S, Nisar L. Friction stir welding of AA2024-T3 and SS304 alloys: microstructural analysis, microhardness evaluation, and tensile performance. *Physica Scripta*. 2024;99(10): 105970.
36. Zhang M, Liu JM, Xue P, Liu FC, Wu LH, Ni DR, Xiao BL, Wang KS, Ma ZY. Eliminating Cu-rich intermetallic compound layer in dissimilar friction stir welding of 304 stainless steel and 2219 Al alloy via ultralow rotation speed. *Journal of Materials Processing Technology*. 2024;329: 118444.
37. Nakrani J, Yan W, Shrivastava A. Fatigue crack growth behavior in SS304-Al5083 dissimilar friction stir welded joints. *Procedia Structural Integrity*. 2024;61: 188–194.
38. Caetano GDQ, Andrade TC, Motta MF, Miranda HC, Farias JP, Bergmann LA, Dos Santos JF, Silva CC. Assessment of the joint configuration and welding parameters for the dissimilar joining of AISI 304L and AISI 410S stainless steels by friction stir welding. *The International Journal of Advanced Manufacturing Technology*. 2024;133: 5691–5703.

39. Kumar A, Bansal SN, Chandraker R. Computational modeling of blast furnace cooling stave based on heat transfer analysis. *Materials Physics and Mechanics*. 2012;15(1): 46–65.
40. Yadav A, Jain A, Verma R. Effect of tilt angle for conical pin tool with a conical shoulder on heat transfer and material flow using numerical simulation in friction stir welding. *Materials Physics and Mechanics*. 2023;51(3): 126–145.
41. Yadav A, Jain A, Verma R. Numerical Simulation of Friction Stir Welding Process to Investigate the Effect of a Conical Pin Tool with a Flat and Conical Shoulder on Heat Transfer. *NanoWorld Journal*. 2023;9(S1): S239–S242.
42. Hasan AF. CFD modelling of friction stir welding (FSW) process of AZ31 magnesium alloy using volume of fluid method. *Journal of Materials Research and Technology*. 2019;8(2): 1819–1827.
43. Yadav A, Jain A, Verma R. Rotational Speed Influence on Weld Temperature in Friction Stir Lap Joint of Aluminium Alloy 6061 Using Numerical Simulation. *Journal of Polymer and Composites*. 2024;12(S02): 235–245.
44. Nandan R, Roy GG, DebRoy T. Numerical simulation of three dimensional heat transfer and plastic flow during friction stir welding. *Metallurgical and Materials Transactions A*. 2006;37(4): 1247–1259.
45. Yang CL, Wu CS, Lv XQ. Numerical analysis of mass transfer and material mixing in friction stir welding of aluminum/magnesium alloys. *Journal of Manufacturing Processes*. 2018;32: 380–394.
46. Nandan R, Roy GG, Lienert TJ, DebRoy T. Numerical modelling of 3D plastic flow and heat transfer during friction stir welding of stainless steel. *Science and Technology of Welding and Joining*. 2006;11(5): 526–537.
47. Thomas WM, Johnson KI, Wiesner CS. Friction stir welding—recent developments in tool and process technologies. *Advanced Engineering Materials*. 2003;5(7): 485–490.
48. Sheppard T, Wright DS. Determination of flow stress: Part 1 constitutive equation for aluminium alloys at elevated temperatures. *Metallurgical Technology*. 1979;6(1): 215–223.
49. Sheppard T, Jackson A. Constitutive equations for use in prediction of flow stress during extrusion of aluminium alloys. *Materials Science and Technology*. 1997;13(3): 203–209.
50. Tello KE, Gerlich AP, Mendez PF. Constants for hot deformation constitutive models for recent experimental data. *Science and Technology of Welding and Joining*. 2010;15(3): 260–266.
51. Hasan AF, Bennett CJ, Shipway PH, Cater S, Martin J. A numerical methodology for predicting tool wear in friction stir welding. *Journal of Materials Processing Technology*. 2017;241: 129–140.
52. Darvazi AR. A semi-analytical solution for temperature distribution in friction stir welding. Research Square [Preprint] 2021. Available from: doi.org/10.21203/rs.3.rs-521499/v1
53. Sadeghian B, Taherizadeh A, Atapour M. Simulation of weld morphology during friction stir welding of aluminum–stainless steel joint. *Journal of Materials Processing Technology*. 2018;259: 96–108.
54. Hamilton C, Dymek S, Sommers A. A thermal model of friction stir welding in aluminum alloys. *International Journal of Machine Tools and Manufacture*. 2008;48(10): 1120–1130.
55. Neto DM, Neto P. Numerical modeling of friction stir welding process: A literature review. *The International Journal of Advanced Manufacturing Technology*. 2013;65: 115–126.
56. Zhang J, Shen Y, Li B, Xu H, Yao X, Kuang B, Gao J. Numerical simulation and experimental investigation on friction stir welding of 6061-T6 aluminum alloy. *Materials & Design*. 2014;60: 94–101.
57. Mishra RS, Ma ZY. Friction stir welding and processing. *Materials Science and Engineering R: Reports*. 2005;50(1–2): 1–78.
58. Mishra RS, Mahoney MW. (Eds.) *Friction Stir Welding and Processing*. Materials Park (OH): ASM International; 2007.
59. Mishra RS, De PS, Kumar N. *Friction Stir Welding and Processing: Science and Engineering*. Berlin: Springer; 2014.
60. Khalafe WH, Sheng EL, Bin Isa MR, Omran AB, Shamsudin SB. The Effect of Friction Stir Welding Parameters on the Weldability of Aluminum Alloys with Similar and Dissimilar Metals: Review. *Metals*. 2022;12(12): 2099.
61. Safeen MW, Russo Spena P. Main Issues in Quality of Friction Stir Welding Joints of Aluminum Alloy and Steel Sheets. *Metals*. 2019;9(5): 610.
62. Schmidt H, Hattel J, Wert J. An analytical model for the heat generation in friction stir welding. *Modelling and Simulation in Materials Science and Engineering*. 2004;12(1): 143–157.
63. Yadav A, Jain A, Verma R. Effect of pin shapes on temperature distribution in friction stir lap joint of AA6061 with AZ31 using numerical simulation. *International Journal of Simulation and Process Modelling*. 2024, 21(4): 251-263.
64. Arora A, Nandan R, Reynolds AP, DebRoy T. Torque, power requirement and stir zone geometry in friction stir welding through modeling and experiments. *Scripta Materialia*. 2009;60(1): 13–16.
65. Ulysse P. Three-dimensional modeling of the friction stir-welding process. *International Journal of Machine Tools and Manufacture*. 2002;42(14): 1549–1557.